Eye-Region Specific Ribbon Tuning Supports Distinct Modes of Synaptic Transmission in Same-Type Cone-Photoreceptors

Cornelius Schröder[1,2,$], Jonathan Oesterle[1,2], Philipp Berens[1,2,3*], Takeshi Yoshimatsu[4*], Tom Baden[1,4*$]

Summary. Many sensory systems use ribbon-type synapses to transmit their signals to downstream circuits. The properties of this synaptic transfer fundamentally dictate which aspects in the original stimulus will be accentuated or suppressed, thereby partially defining the detection limits of the circuit. Accordingly, sensory neurons have evolved a wide variety of ribbon geometries and vesicle pool properties to best support their diverse functional requirements. However, the need for diverse synaptic functions does not only arise across neuron types, but also *within*. Here we show that UV-cones, a single type of photoreceptor of the larval zebrafish eye, exhibit striking differences in their synaptic ultrastructure and consequent calcium to glutamate transfer function depending on their location in the eye. We arrive at this conclusion by combining serial section electron microscopy and simultaneous "dual-colour" 2-photon imaging of calcium and glutamate signals from the same synapse *in vivo*. We further use the functional dataset to fit a cascade-like model of the ribbon synapse with different vesicle pool sizes, transfer rates and other synaptic properties. Exploiting recent developments in simulation-based inference, we obtain full posterior estimates for the parameters and compare these across different retinal regions. The model enables us to extrapolate to new stimuli and to systematically investigate different response behaviours of various ribbon configurations. We also provide an interactive, easy-to-use version of this model as an online tool. Overall, we show that already on the synaptic level of single neuron types there exist highly specialized mechanisms which are advantageous for the encoding of different visual features.

1: Institute for Ophthalmic Research, University of Tübingen, Germany; 2: Center for Integrative Neuroscience, University of Tübingen, Germany; 3: Bernstein Center for Computational Neuroscience, Centre for Integrative Neuroscience, all: University of Tübingen, Germany; 4: School of Life Sciences, University of Sussex, UK; *equally contributing senior authors; $Correspondence: cornelius.schroeder@uni-tuebingen.de; t.baden@sussex.ac.uk.

AUTHOR CONTRIBUTIONS. The manuscript was conceptualised and developed by CS, TY, TB and PB. CS established the models and together with JO adapted the inference method. TY performed electron microscopy and two-photon imaging, pre-processing of the data and generated transgenic lines, with support from TB. CS performed additional analyses and statistical testing, with help from PB. TB and PB supervised the project. The manuscript was written by CS and TB with input from TY and PB. Funding was acquired by TB, PB and TY.

DECLARATION OF INTERESTS. The authors declare no competing interests.

INTRODUCTION

Ribbon-type synapses feed high-bandwidth sensory signals into their postsynaptic networks (reviewed in e.g. (Moser et al., 2019; Sterling and Matthews, 2005)). However, depending on the species, modality, or receptor type the nature of this synaptic transfer can differ greatly. For example, auditory systems typically operate at higher frequencies than visual systems, and accordingly auditory inner hair cells tend to use "faster" ribbon synapses compared to those of photoreceptors (Baden et al., 2013a; Moser et al., 2019). Moreover, amongst photoreceptors of the vertebrate eye, rods and cones tend to differ greatly in the way they use their ribbons (Regus-Leidig and Brandstätter, 2012; Sterling and Matthews, 2005). Rods generally have large ribbons that can dock many hundreds of vesicles at a time, concentrated at a single release site, to support focussed, low-noise transmission (e.g. (Hays et al., 2021)). In contrast, cones usually use multiple smaller ribbons, often positioned at different release sites in a single pedicle, to serve diverse postsynaptic circuits (e.g. (DeVries et al., 2006; Jackman et al., 2009)). The ribbon synapses in electrosensory organs of elasmobranchs take such ribbon tuning to the extreme (Bellono et al., 2018). For example, sharks achieve high-amplitude pulsative transmission required for predation by combining greatly elongated ribbons with an ion-channel composition that supports broad spiking. In contrast, skates drive their smaller ribbons using graded voltage signals to support low-amplitude, oscillatory transmission suitable for intraspecific communication. Clearly, ribbons and their associated molecular machinery are key structural tuning sites of synaptic function in many sensory systems.

However, the functional requirements of synaptic transmission do not only differ across neuron types, but also *within* (Baden et al., 2018, 2013b; Franceschini et al., 1981; Sinha et al., 2017; Szatko et al., 2019; Yoshimatsu et al., 2020b). For example, in vision, different parts of the eye survey different parts of visual space, often with distinct distribution of light and visuo-ecological significance (reviewed in (Baden et al., 2020; Land et al., 2012)). Correspondingly, we hypothesised that within-type functional tuning of a sensory receptor neuron should also utilise the vast tuning potential of its ribbon.

We explored this idea on the model of larval zebrafish UV-cone photoreceptors, which exhibit profound structural, molecular and circuit differences depending on their location in the eye (Yoshimatsu et al., 2020b). UV-cones in the acute zone (AZ) combine an enlarged outer segment with molecular tuning of the phototransduction cascade, an elevated calcium baseline and strong feedback from horizontal cells to boost detection brighter-than-background stimuli. This serves to support visual prey capture of UV-bright water-borne micro-organisms such as paramecia. In contrast, UV-cones in other parts of the eye preferentially respond to darker-than-background stimuli, which may serve silhouette detection of nearby objects against the backdrop of bright UV-scatter

2

from the sun. Amongst themselves, non-AZ UV cones further differ in additional aspects, including their absolute light sensitivity. Building on these earlier results, we here asked if and how the actual synaptic transfer differs amongst UV-cones across the eye.

First, we used electron microscopy to reveal eye-region specific structural differences amongst UV-cone ribbons and their presynaptic distribution of vesicles. Next, we found kinetic differences in synaptic transfer using *in-vivo* simultaneous dual-colour 2-photon imaging of the same pedicles' presynaptic calcium and resultant release. We then tied these findings together in a biophysical model, which enables computationally exploring possible underlying biological mechanisms and sites of tuning within the release cascade. Finally, we generalised our findings into an online model of synaptic transfer from the ribbon that enables free control over all key parameters, including ribbon dimensions, their dynamics, and the behaviour of underlying calcium drive (available online at http://www.tinyurl.com/h3avl1ga).

RESULTS

UV-cone ribbon geometry and vesicle distributions differ with eye position. To establish possible structural differences amongst larval zebrafish UV-cone ribbon synapses, we obtained volumetric electron microscopy datasets of the outer retina taken from three different regions: Acute zone (AZ), Nasal (N) and Dorsal (D). For each region, we anatomically identified (Yoshimatsu et al., 2020a) and 3D-reconstructed UV-cone pedicles ($n_{AZ, N, D}$ = 6, 6, 6) including their full complement of ribbons and surrounding vesicles (Fig. 1a-c, Methods). This revealed that dorsal ribbons were smaller (Fig. 1d,e) and less numerous (Fig. 1f) compared to AZ or nasal ones. However, nasal UV-cones had the lowest vesicle density immediately adjacent to the ribbon (Fig. 1g, Fig. S1). In addition, further away from the ribbon, the vesicle density was lowest in dorsal UV-cones, and highest in AZ UV-cones (Fig. 1g, Fig. S1). Taken together, the overall complement between ribbon number, geometry and vesicle distributions therefore markedly differed across the three regions of the eye (Fig. 1h). We next asked if and how these structural differences may translate into differences in synaptic function.
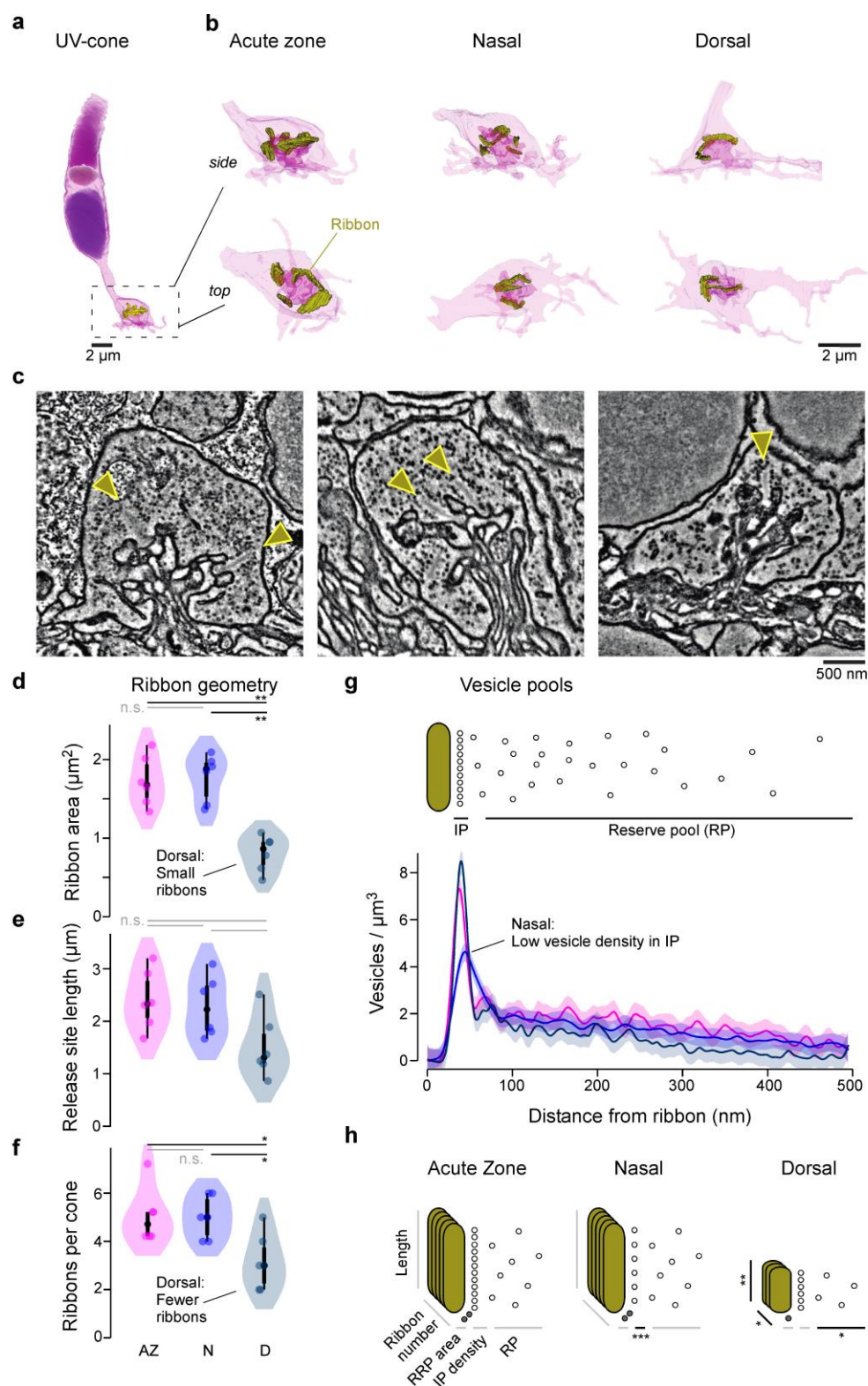
3

Figure 1. Eye-region-specific structural tuning of a ribbon synapse in UV-cones. a, Example of a full UV-cone reconstruction, taken from the acute zone. Dark purple: nucleus, light-purple: mitochondria, purple: outer segment, yellow: ribbon. **b,** Zoom-ins of UV-cone terminals from different regions with ribbons highlighted in yellow, each shown from the side (top) and from below (bottom). **c** Example electron-microscopy images from each zone, with arrowheads indicating ribbons. **d,e,f** Violin plots of the ribbon geometry and number for the three different regions (two-sided shuffling test with Bonferroni correction, n_{AZ}, n_N, n_D = 6, 6, 6, * $p<0.05$, ** $p< 0.01$). **g** Two-dimensional schema of the vesicle pools at a ribbon synapse and vesicle densities as a function of distance to the ribbon (see Fig. S1 for statistics). **h,** Summary schema of observed EM-level differences between UV-cones at the level of ribbon geometry, number, and vesicle distributions, when compared to AZ.

147 **Eye-region dependent differences in UV-cone release kinetics**. To
148 simultaneously monitor presynaptic calcium and resultant glutamate
149 release from single UV-cone pedicles *in vivo*, we expressed the "green"
150 fluorescent glutamate biosensor SFiGluSnFR in horizontal cells
151 postsynaptic to the cones, and the "red" calcium biosensor SyjRGeco1b
152 in all-cones (Fig. 2a,b, Methods). UV-cones were unambiguously
153 identified based on their robust responses only to UV-light (Methods,
154 (Yoshimatsu et al., 2020a)). We then concurrently recorded red and
155 green fluorescence signals under two-photon during presentation of
156 100% contrast widefield flashes of UV-light (3 s On, 3 s Off), starting
157 from a 50% contrast background (Fig. 2c, Methods). In example
158 recordings from each eye region, this revealed very different glutamate
159 signals during light offsets, despite similar calcium signals (Fig. 2c).
160 When scaled to their common sustained component, the dorsal cone
161 was much more transient compared to the nasal cone, with a kinetically
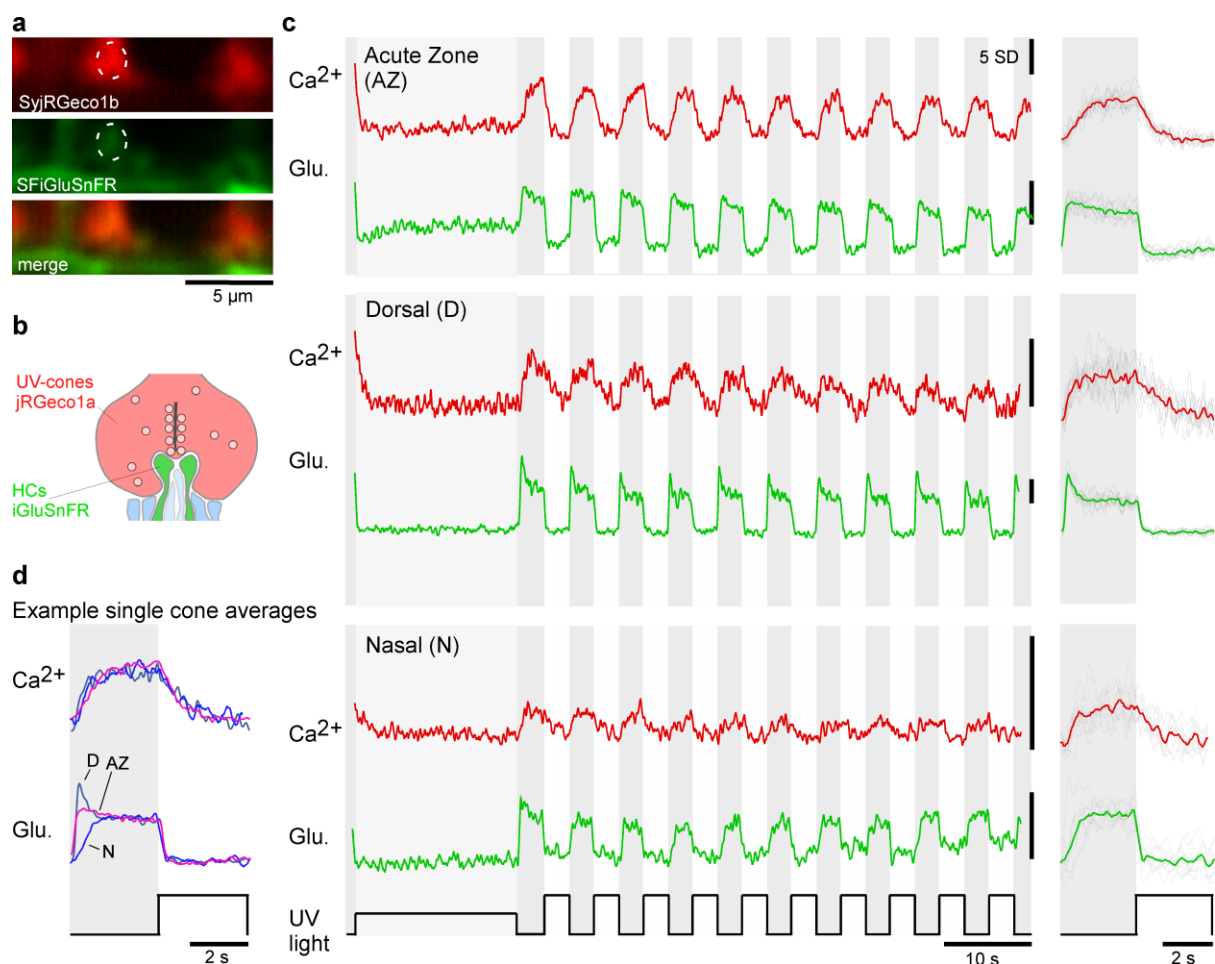162 intermediate AZ-cone (Fig. 2d).

163

164 ***Figure 2. Simultaneous in vivo imaging of synaptic calcium and release. a,b*** *Simultaneously acquired two-*
165 *photon scans of cone terminals and opposing horizontal cell dendrites, with cone-pedicles expressing*
166 *SyjRGeco1b (red), and horizontal cell dendrites expressing SFiGluSnFR (green), and schematic representation,*
167 *showing the cone-pedicle (red) with ribbon and vesicles, as well as horizontal cell processes (green) and bipolar*
168 *cell dendrites (blue).* ***c,*** *Examples of raw calcium (red) and glutamate (green) traces recorded simultaneously*
169 *from single UV-cones, one from each eye region as indicated. The averaged traces, and superimposed stimulus*
170 *repetitions are shown on the right* ***d,*** *Overlay of the averaged traces in (c), highlighting different glutamate*
171 *responses despite very similar calcium responses.*

172   To systematically test for consistent differences between synaptic
173   transfer in the three eye regions, we recorded paired calcium and
174   glutamate signals from a total of n = 30, 16, 9 AZ, dorsal and nasal UV-
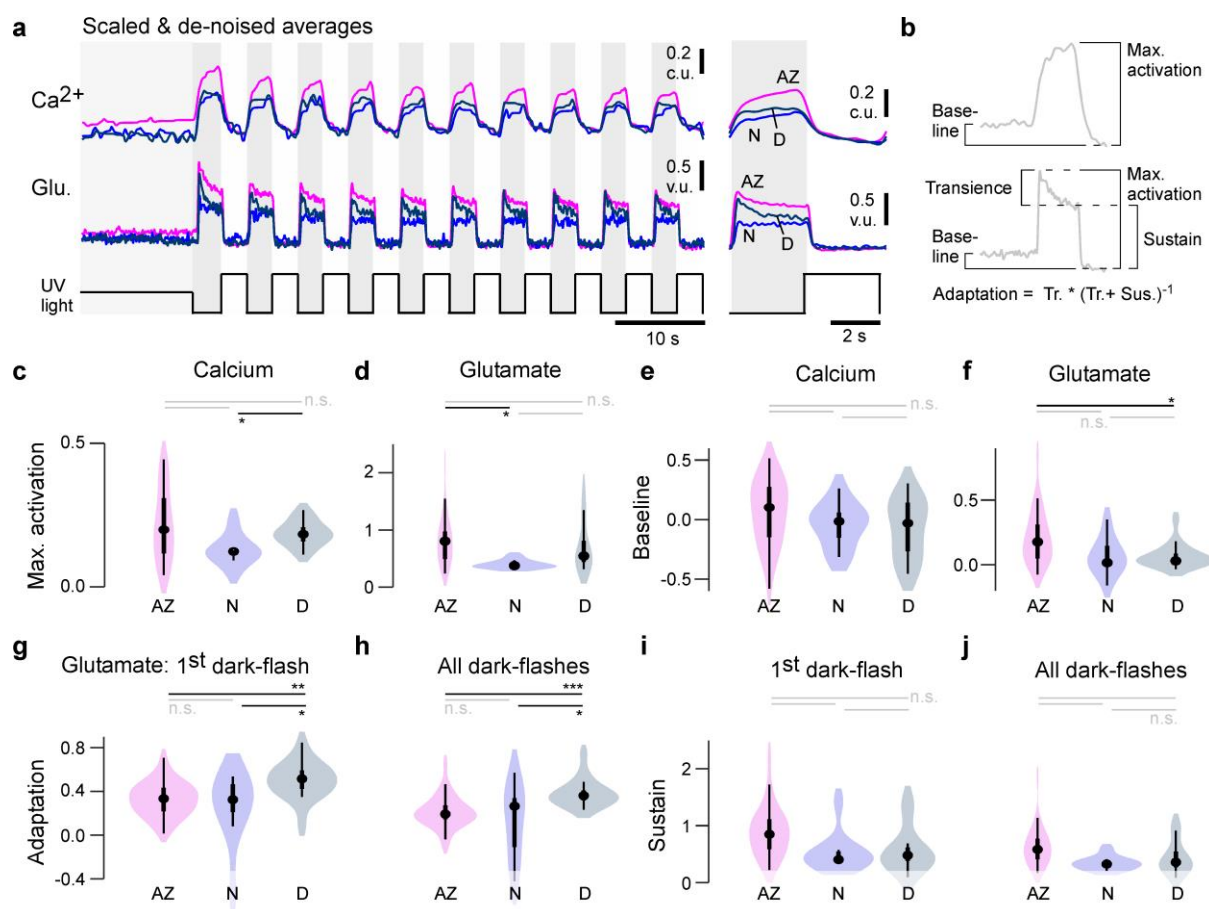175   cones, respectively (Fig. S2).

176

Figure 3. Physiological differences in light responses between UV-cones from different eye-regions. a, *Scaled and de-noised calcium and glutamate recordings averaged across multiple ROIs (Methods). The traces shown also serve as input for the biophysical model (see Fig. 4). b, Schema of the calculated indices in (c-j) (Methods). The transience index is computed as $\frac{max. - sustain}{max.}$. c-j, quantification of physiological differences for the three different retinal regions (two-sided shuffling test with Bonferroni correction, n_{AZ}, n_N, n_D = 30,9,16, * p<0.05, ** p< 0.01, *** p<0.001).*

183   We then scaled and de-noised each recording (Methods) and computed
184   the mean traces (Fig. 3a) as well as key parameters relating to the
185   amplitudes and kinetics of calcium and glutamate signals (Fig. 3b-j). For
186   this, all traces where normalized with respect to the UV-bright stimulus
187   periods, which we previously showed correspond to the lowest possible
188   calcium and glutamate release at the stimulus brightness used
189   (Yoshimatsu et al., 2020b). We then computed several indices of
190   calcium and glutamate response amplitudes and their kinetics (Fig. 3b),
191   which together confirmed and extended initial observations from the
192   single-pedicle examples (cf. Fig. 2). In particular, both at the level of
193   calcium (Fig. 3c) and glutamate (Fig. 3d), nasal UV-cones exhibited
194   small peak-amplitudes. In addition, the glutamate release baseline of AZ
195   UV-cones was increased during 50% contrast at the start of the stimulus
196   (Fig. 3f). In line with previous work, the AZ calcium baseline also

6

appeared elevated (Fig. 3a), however this difference was not statistically significant (Fig. 3e). This was likely related to the lower signal-to-noise ratio of jRGeco1b signals, compared to those of GCaMP6f as used previously (Yoshimatsu et al., 2020b). Next, we quantified amplitudes of transient and sustained components at the level of glutamate (Fig. 3b,g-j). For this, we analysed the first flash response separately from the mean of subsequent ones because all regions exhibited notably stronger adaptation during the first flash (Fig. 3a). Overall, this consistently revealed the most pronounced within-pulse adaptation in dorsal UV-cones (Fig. 3g,h), alongside possible but and non-statistically significant differences amongst sustained components (Fig. 3i,j). Taken together, our results so far highlight a range of structural (Fig. 1) and functional (Figs. 2,3) differences in the synaptic machinery of UV-cones across different regions of the eye.

A model of glutamate release at the ribbon synapse. To systematically explore the possible mechanistic basis of the observed eye-wide variations in UV-cone synaptic functions, we next modelled the release machinery of the ribbon with a biophysical interpretable model that converts calcium signals to glutamate release (Baden et al., 2014; Schröder et al., 2019). The model consisted of three different vesicle pools (reserve pool (RP), intermediate pool (IP) and readily releasable pool (RRP)), the changing rates between these pools (J^{RP_IP}, J^{IP_RRP}, J^{Exo}) and a sigmoidal non-linearity with slope k and offset $x0$ which drives the final release (Fig. 4a, Methods). Building on recent advances in simulation-based Bayesian inference (Gonçalves et al., 2020; Lueckmann et al., 2017), we estimated posterior distributions over the model parameters using a loss function capturing essential components of the release dynamics (Fig. 4b, Methods). The model fitted the functional data well and accurately modelled the pronounced first UV-flash response differences between zones (Fig. 4c). From here, the inferred posteriors (see Fig. S3a for two dimensional marginals) allowed us to compare the likely parameters between the different zones, including the estimated uncertainties. This allowed pinpointing possible key differences: For example, the calcium offset (x_0, which can be understood as the inverted calcium baseline, Methods) was markedly increased in the nasal model (Fig. 4d,e). In contrast, in case of maximal release rate, the posterior for the nasal data stayed close to the prior, indicating that this parameter was not essential to reproduce the traces. For RRP sizes and associated maximal refill rates the model required the smallest values nasally (Fig. 4e). Interestingly, with few exceptions (e.g. the maximal release rate and calcium offset), the parameter posteriors were mostly uncorrelated (Fig. S3a), indicating that the model and data leave little room for possible compensatory mechanisms.
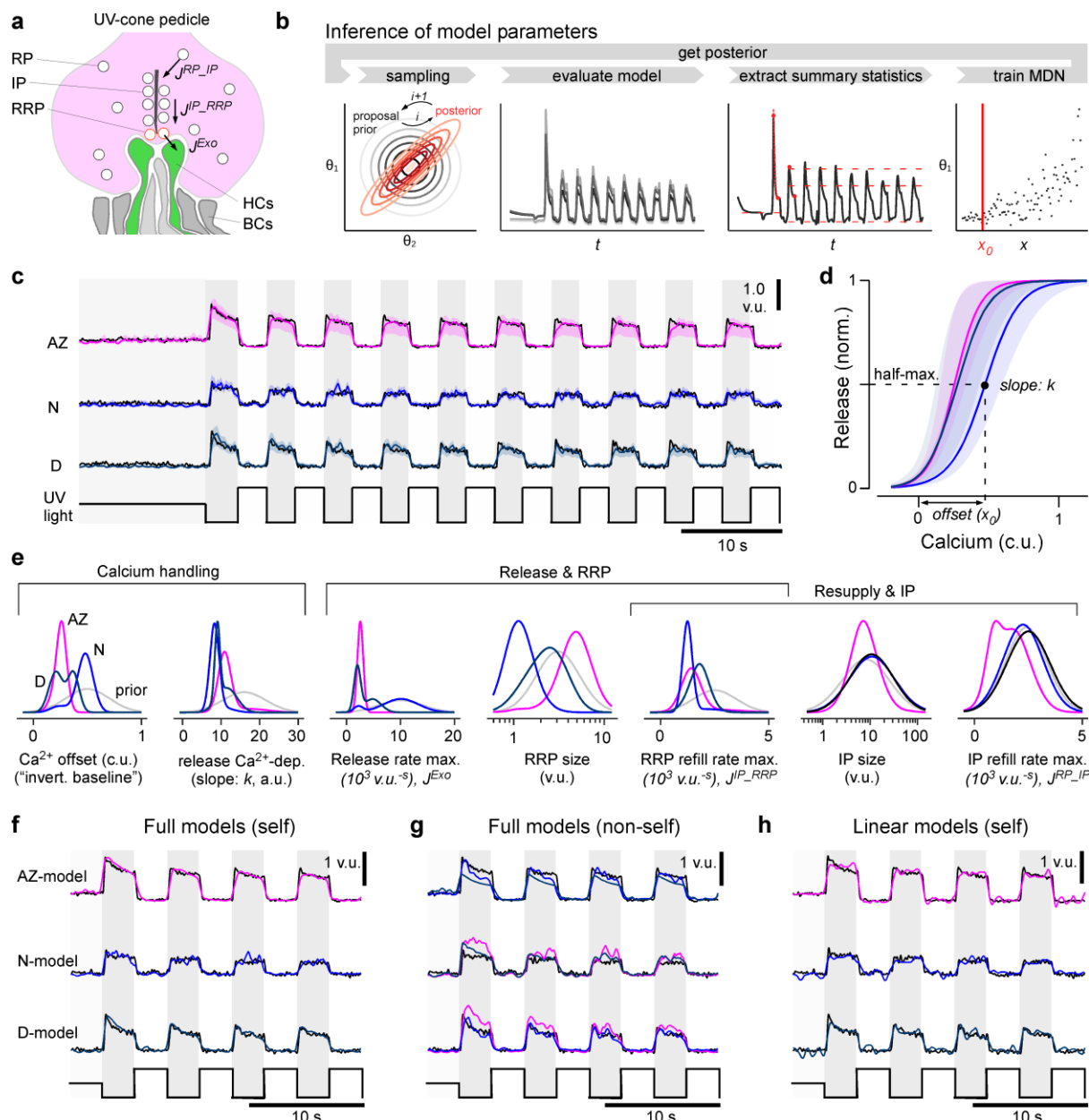
Figure 4. A model of calcium evoked release from the ribbon. a, Schema of the movement of vesicles at a ribbon synapse. The vesicles move from the reserve pool (RP) to the intermediate pool (IP) at the ribbon and finally to the readily releasable pool (RRP) close to the membrane before they are released into the synaptic cleft to activate the dendrites of invaginating horizontal cells (HC). **b,** Schema of the parameter inference: Over several rounds, samples are first drawn from a prior, the model is then evaluated and summary statistics on which the loss function is calculated are extracted. Based on these values and the sampled parameters a mixture of density network (MDN) is trained and evaluated to get the posterior / prior for the next round. **c,** Model predictions for the three regions (mode and 90% prediction intervals from posterior samples in colour, data in black). **d,** Mode and 90% prediction intervals of the model's non-linearity. **e,** Prior and one-dimensional marginals of the posterior distributions (see Fig. S3a for the two-dimensional marginals). The units are vesicle units (v.u.) and calcium units (c.u.), referring to the scale invariance of the model. **f,** Evaluation of the best region- specific models on its region-specific calcium traces. **g,** Evaluation of best region- specific model on the calcium races of the other regions. **h,** Evaluation of the linear baseline model (model in colour, data in black): especially the transient components are missed.

To confirm that the different model outputs do not simply rely on differences in the calcium inputs but rather on the differences of the inferred parameters, we compared the performance of the zone-specific models by shuffling the inferred parameters and glutamate datasets

8

260 pairwise across zones (Fig. 4f,g). The match between the model output
261 and measured glutamate release for a calcium input was generally
262 worse for parameters corresponding to a different region, confirming
263 that our release models were indeed regionally specific. For example,
264 the sustained component of the AZ could not be captured by either the
265 dorsal or nasal models (Fig. 4g). Moreover, the models produced
266 different transient behaviours independent of the calcium inputs (Fig.
267 4f,g). The shuffled models also achieved lower loss when evaluated on
268 self-, compared to non-self calcium inputs (Fig. S3b,c). Additionally, we
269 compared the biophysical model to a statistical linear baseline model
270 (Methods). While as expected the linear model captured the general
271 shape of the flash responses, it was not able to model glutamate
272 transients nor adaptation over several flashes (Fig. 4h). This also
273 resulted in much higher loss values for the question-specific loss
274 function as well as for the mean squared error of the glutamate traces
275 (MSE, Fig. S3b,c). Together, this confirmed the general validity of our
276 modelling approach, suggesting that the posterior distributions of each
277 regional model can usefully inform about the differences that underpin
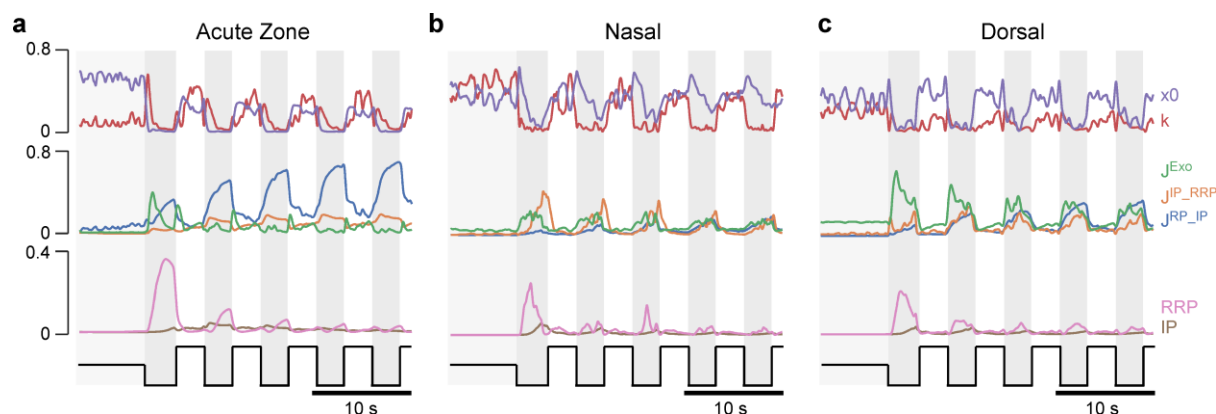278 region-specific transfer functions from synaptic calcium to release via
279 the ribbon.

280

281 **Figure 5. Sobol Indices. a-c,** *Sensitivity of the model for the different model parameters measured by the Sobol*
282 *Index (Methods). The Sobol Index measures the expected reduction in relative variance for the fixation of*
283 *parameter θ_i. It depends on the posterior distribution and is therefore different for the fits to the three regions.*

284 **Predicting region-specific processes**. An important strength of our
285 modelling approach was that it allowed systematically exploring the
286 possible influence of parameters such as vesicle pool sizes, their
287 vesicle movements, and their calcium dependence, on the model
288 output. To this end, we conducted a sensitivity analysis by computing
289 the first order Sobol indices (Methods), a measure of the direct effect of
290 each parameter on the variance of the model output.

291 This revealed a generally high influence of the calcium parameters (*x0*
292 and *k*) during UV-bright periods and around light-dark transitions in all
293 three zones (Fig. 5a-c, top row). In contrast, beyond an initial key role of
294 the RRP size for shaping the first dark-flash response, pool sizes
295 generally played only relatively minor roles (Fig. 5, bottom row). Instead,
296 the most obvious region-wise differences occurred amongst vesicle

9

297 transition rates between the pools. For example, the refilling rate of the
298 IP from the RP ($J^{RP\text{–}IP}$) was increasingly critical for shaping dark flash
299 responses in the AZ-model (Fig. 5a, blue) but had comparatively little
300 influence in the nasal model (Fig. 5b, blue). In contrast, the maximal
301 release rate (J^{Exo}) particularly influenced the variance in early dark flash
302 responses in the dorsal model (Fig. 5c, green), while nasally refilling of
303 the RRP from the IP ($J^{IP\text{–}RRP}$) played a greater role (Fig. 5b, yellow).
304 Together, this analysis suggests that particularly the rates of vesicle
305 transfer between pools, rather than the pool sizes themselves or their
306 calcium dependence, may underpin the experimentally observed region
307 wise differences in release properties from zebrafish UV-cones *in vivo.*

308 **General rules of ribbon tuning.** We next sought to explore the general
309 parameter landscape underlying release from the ribbon. For this, we
310 calculated the same indices as in the corresponding data from 2P
311 imaging (Fig. 3), but this time on the model output obtained by
312 simulating the model with parameters drawn from the posterior
313 distributions. As expected, this reproduced the trends previously
314 measured *in vivo*, including the low maximal activation nasally (Fig. 6a),
315 the largest transient component dorsally (Fig. 6b), and the largest
316 sustained component in the AZ (Fig. 6c).

317 From here, we simplified the model by fixing the slope of the calcium
318 non-linearity (*k*) and defining vesicle change rates as fractions of the
319 corresponding pool sizes (Methods). To be able to stimulate the model
320 with arbitrary "light" stimuli, we moreover implemented a linear calcium
321 model based on a convolution with a biphasic kernel to reflect cone-
322 activation by light (Schnapf and Baylor, 1987), and monophasic kernel
323 to reflect calcium kinetics (Baden et al., 2014). This latter kernel was
324 varied in subsequent simulations to explore the impact of calcium
325 kinetics on synaptic performance (Methods). Together, this allowed us
326 to reduce the parameter space while at the same time identifying
327 underlying computational principles. In the following, we always
328 included the three fitted eye-region specific parameter sets as a point of
329 comparison (coloured "dots" on top of heatmaps in Figs. 6,7). These
330 dots should be treated with some caution, since in the simplified model
331 they do not necessarily match the original ones in every dimension.

332 Exploring this model (Fig. 6d-f), we found that both maximal activation
333 (Fig. 6d) and the size of the sustained component (Fig. 6f) could be
334 tuned by varying RRP and/or IP pool sizes (left column), with negligible
335 contributions from the maximal release rate or the calcium offset (right
336 column). In contrast, the transient component primarily hinged on the
337 maximal release rate (Fig. 6e, right column), with more complex
338 additional contributions from the interplay of vesicle pool sizes (left
339 column). Accordingly, our generalised model suggests that transient
340 and sustained responses can be defined largely non-overlapping
341 properties of the ribbon, possibly providing a powerful handle in for their

342   independent tuning. For further exploration, the full model is available
343   online as an interactive tool (Fig. 6g):
344   *google colab* (http://www.tinyurl.com/h3avl1ga).
345   *github* (https://github.com/coschroeder/cone_ribbon).
346

347
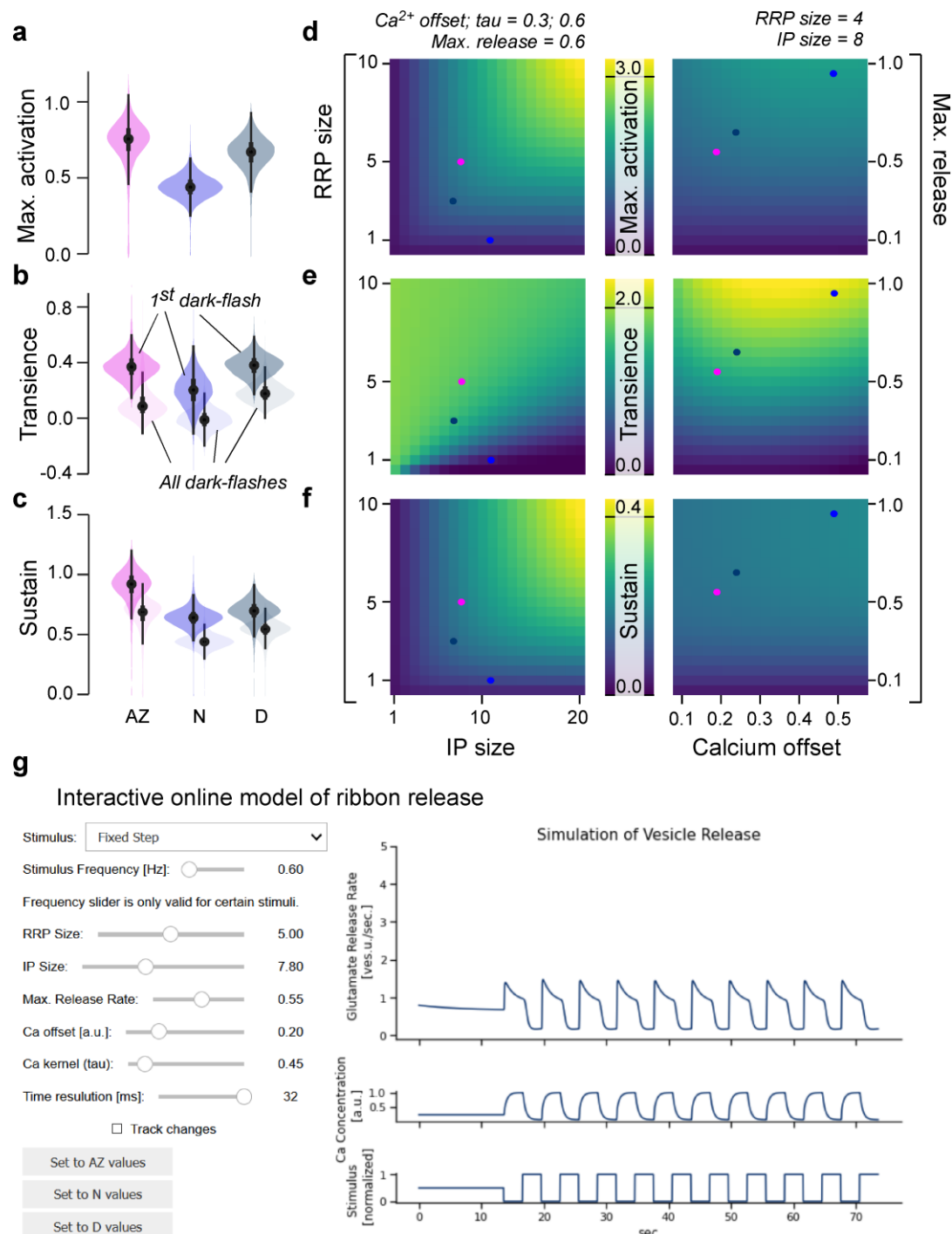
Figure 6. General rules of ribbon tuning: Basic response parameters. a-c. *The same indices as in* Fig. 3, *but here calculated on 10,000 model evaluations on samples from the posteriors. The model has learned the differences between the retinal regions and reproduces these differences (see* Fig. 3 *for comparison).* **d-f,** *Indices as in (a-c), calculated on different parameter combinations as indicated. For this analysis, a step-stimulus feeding into a linear calcium model was added as the input to the release model (Methods). For definition of the indices see also* Fig. 3b. **g,** *Screenshot of the interactive online model, available at* http://www.tinyurl.com/h3avl1ga.

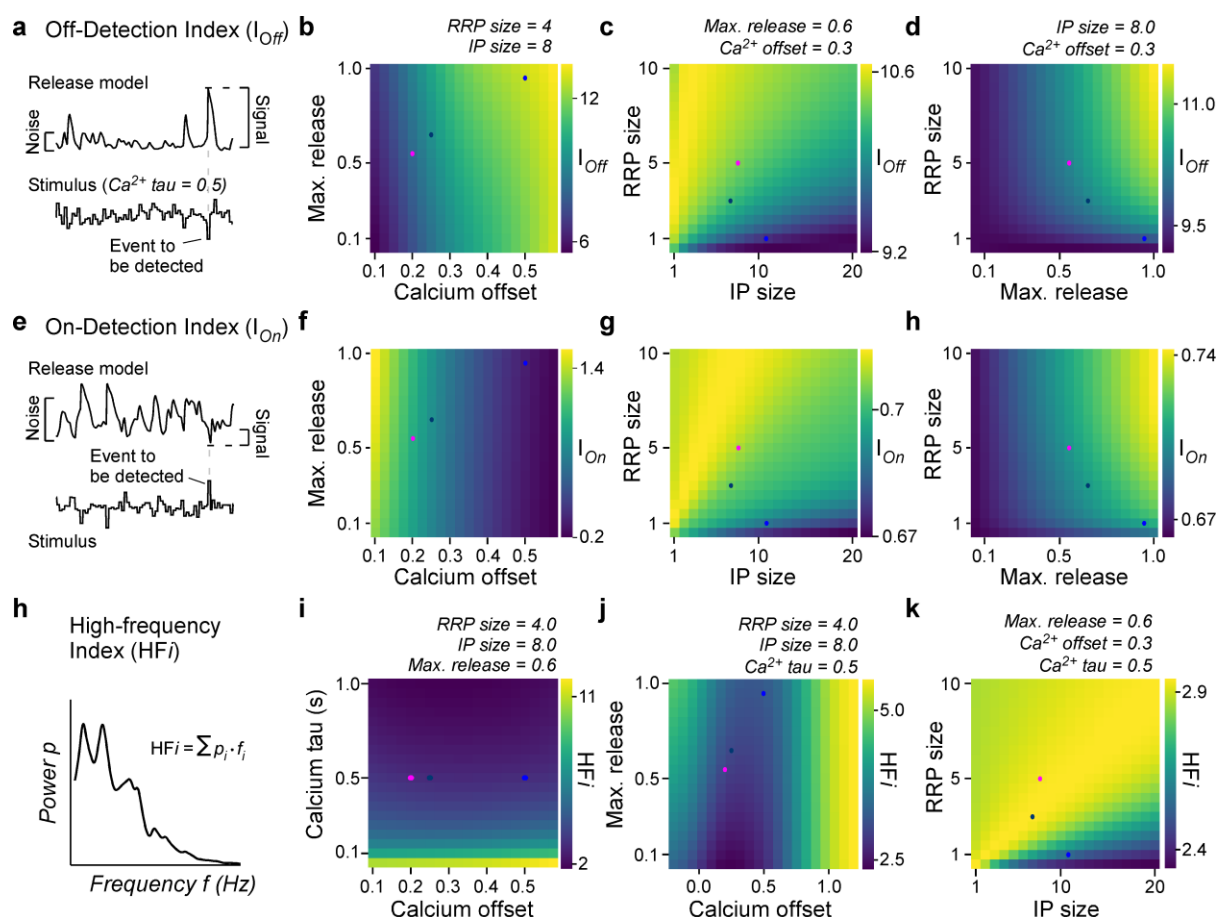**Figure 7. General rules of ribbon tuning: Event detection and high-frequency encoding. a,** *An Off-Detection index (I_{Off}) measures the model's baseline-noise normalised response amplitude to an Off-event in the stimulus as indicated (Methods).* **b-d** *I_{Off} for different parameter combinations.* **e-h,** *as (a-d), but for an On-detection index (I_{On}).* **h,** *The high-frequency index (HFi) is a weighted sum of the discretized power spectrum and indicates the behaviour in a high frequency regime.* **i-k,** *HFi for different parameter combinations. The fixed parameters are shown as titles in each panel. Note the different colour scales between panels. Further note that in (j) we explored the x_0 parameter space up to extreme response behaviour, which may not be physiologically plausible.*

Frequency dependence and event detection. In a final step, we explored the model behaviour on new stimuli and investigated the influence of the model parameters on different coding properties of the synapse. First, we measured the detectability of a high amplitude dark-event amongst an otherwise noisy stimulus sequence (Fig. 7a, Methods). This highlighted the calcium offset (x_0) as a key parameter (Fig. 7b). Once x_0 is set, additional benefits could be gained from increasing RRP-size but only small benefits from increasing IP size (Fig. 7c), ideally in further combination with a high maximal release rate (Fig. 7d). We next measured the detectability of light-events in the same way (Fig. 7e, Methods). This showed that beyond an inverse dependence on calcium baseline (Fig. 7f cf. Fig. 7b), the ribbon parameters that benefitted the detection of On- and Off-events were in fact virtually identical (Fig. 7g,h, cf. Fig. 7c,d). The low calcium offset (i.e. high baseline) supporting the detection of On-events is in line with our previous work (Yoshimatsu et al., 2020b), where the AZ showed highest

12

380
381
calcium baseline and an enhanced ability to detect visuo-ecologically important UV-On events such as the presence of prey.

382
383
384
385
386
387
388
389
Finally, we explored how well different ribbon models could transmit fast temporal flicker, here summarised by a high-frequency index (HF*i*) (Fig. 7h, Methods). This revealed that this property primarily depended on the calcium kinetics, rather than the specific tuning of the ribbon itself (Fig. 7i-k). Beyond calcium dynamics (here, fixing calcium *T* at 0.5 s), again the calcium offset (Fig. 7j) as well as an approximate balance of medium-sized pools for both the RRP and IP (Fig. 7k), could provide additional support for encoding high-frequency components.

390

391
DISCUSSION

392
393
394
395
396
397
398
399
400
401
402
Combining ultrastructural evidence (Fig. 1), *in vivo* dual-colour 2-photon imaging (Figs. 2,3) and computational modelling (Figs. 4,5) we have shown how ribbon synapses belonging to the same neuron type can be regionally tuned to support distinct synaptic transfer functions depending on their location in the eye. Our findings complement and extend our recent demonstration that also upstream properties of these UV-cones, are regionally tuned to support different visuo-ecological functions (Yoshimatsu et al., 2020b). We then further generalised this model to explore how specific properties ribbon function can be principally used and traded off against one another to achieve a broad range of synaptic properties (Fig. 6,7).

403
404
405
406
407
408
409
410
411
412
413
414
415
416
417
418
419
Linking ribbon structure and function. Our findings that both UV-cone ribbon ultrastructure (Fig. 1) and their effective synaptic transfer (Fig. 2,3) systematically differed between regions supports the notion that these two sets of properties are linked (Regus-Leidig and Brandstätter, 2012; Sterling and Matthews, 2005; Wichmann and Moser, 2015). However, building a direct bridge between them remains difficult. This difficulty is part related to the absence of a direct experimental link between our EM- and 2P-datasets, which we did not attempt in view of its extreme technical challenges (Holler et al., 2021) that to our knowledge have not been overcome for any ribbon synapse. Moreover, there is often more than one possible interpretation between a finding from EM and its functional consequence. For example, the size of a ribbon is expected to be linked to the number of vesicles it can hold. However, this link presumes that ribbon-attached vesicle density is fixed, which may not be the case, for example due to conceivable variations in available binding sites, or amongst vesicle-transfer rates between pools (e.g. Fig. 4).

420
421
422
423
Such possible complexity is illustrated in case of UV-cone regional variations: For example, dorsal ribbons were by far the smallest and least numerous, which was further complemented by a notable (though non-statistically significant) reduction in release length size (Fig. 1d,e,f).

From here, it is tempting to speculate that therefore their effective IP size, and perhaps also their RRP size, might be comparatively small. However, dorsal UV-cones also had a particularly high vesicle density near the ribbon, while instead nasal UV-cones had markedly reduced vesicle density here despite their otherwise large ribbons (Fig. 1g, Fig. S1). This strongly suggest that looking at ribbon geometry alone may be insufficient to accurately predict effective pool sizes. Instead, joint consideration of ribbon area and vesicle density may be more informative as supported by our model, which produced a near-identical IP size and generally low RRP sizes for both nasal- and dorsal UV-cones (Fig. 4e). In agreement, AZ-cones combined large ribbons with a high vesicle density near the ribbon, and in their case the model did predict the largest RRP size (though a similar IP size). Notably, model IP sizes generally stayed near the prior (Fig. 4e) and exhibited low Sobol indices (Fig. 5), which suggests that this property was not critical for explaining the glutamate responses to our relatively slow and simple test stimulus which was necessitated by the generally low SNR of jRGeco1b signals (Fig. 2). It remains possible that regionally distinct IP-size estimates would emerge in response when fitted to responses to different stimuli.

Beyond ribbon sizes, our ultrastructural analysis further highlighted an elevated vesicle density further away from the ribbon in AZ UV-cones (Fig. 1g, Fig. S1), potentially indicative of an increased RP and/or an increased rate of IP refilling. However, the model produced only minor differences in IP refill rates between regions (Fig. 4e), and for simplicity RP size was fixed because it did not strongly affect function within the tens of seconds timescales interrogated (Baden et al., 2014). Accordingly, a direct link between UV-cone RP vesicle density and function remains outstanding. Conceivably, this property could be helpful for supporting the particularly high total vesicle turnover in AZ-cones (Fig. 3d,f,i) at longer timescales.

At the level of measured function, dorsal cones stood out in that their release was particularly transient (Fig. 3a,g,h) as would be suited for pulsatile, rather than continuous transmission. Their generally small but densely populated ribbons and small RP may be well suited to support this property. In possible agreement, the model predicted a faster RRP refill rate in dorsal cones, which might be useful to ensure the RRP is rapidly replenished after each pulse. Conversely, the effective absence of any transient component nasal UV-cones (Fig. 3a,g,h) in the model resulted in the lowest RRP refill rate, which may further link to the abovementioned low IP occupancy in nasal UV-cones, as observed under EM (Fig. 1g). Moreover, the nasal model simultaneously predicted the smallest RRP but the largest RRP release rate, which resulted in a situation where the very few vesicles ready for release were immediately dumped, thus preventing the build-up of vesicles that enable the transients of dorsal and AZ UV-cones.

Taken together, while it remains difficult to make definitive links between ribbon structure and function, a number of inferences can be drawn which may usefully inform our understanding of the ribbon's role in moulding synaptic transmission to specific needs.

Model and simulation-based inference. The presented model (Fig. 4a) is a modified version of the basic framework used in (Baden et al., 2014). Here we extended the approach by combining simulation-based inference with simultaneous calcium and glutamate recordings to extensively expand the analysis of the model. Moreover, rather than modelling discrete vesicle movements as in (Schröder et al., 2019), our continuous model enabled the use of available software toolboxes (Methods). With the simulation-based inference approach (Fig. 4b) we obtained full posterior distributions (Fig. 4e) rather than point estimates which can lead to overconfident or incorrect conclusions in the case of an under-constrained model or "sloppy" model parameters. At the same time, posterior estimates can be seen as a global method to identify sloppy and stiff parameters (in contrast to local methods as in (Gutenkunst et al., 2007)), and additionally allowed us to conduct a sensitivity analysis by computing the first Sobol indices (Fig. 5). These focus on the variance of the model output rather than on the variance of the posterior distributions and showed zone dependent, biologically interpretable time courses. Finally, by establishing an interactive online model we encourage further exploration of the model and testing of hypotheses.

General rules of ribbon tuning. Bringing together the model and observed differences in response behaviour, we tested our model on new stimuli and computed indices (Fig. 7) which might be relevant to a broad range of sensory scenarios. For all investigated properties, we observed that the baseline and dynamics of the calcium signal were critical (Fig. 7b,f,i), whereupon the anatomical ribbon properties allowed fine-tuning the final output behaviour (Fig. 7c,g,k).

Interestingly, the influence of the calcium baseline for the detection of high-frequency events followed a bimodal distribution (Fig. 7j) with intermediate values offering the poorest performance. In combination with the approximately equal and opposite effects of calcium baseline on the detectability of On- and Off-events (Fig. 7b,f), this suggest that the calcium baseline may present a key variable that enables ribbons to trade-off the transmission of high frequency stimuli against providing an approximately balanced On- and Off- response behaviour. Vice versa, it also suggests that the transmission of high-frequency events benefits from the use of a highly non-linear synapse that is either balanced to On- or Off-events, but not both.

Finally, and perhaps unsurprisingly, the time-course of calcium decay was pivotal for defining the possible working range of high-frequency transmission regardless of the properties of the ribbon itself (Fig. 7i, cf.

15

Fig. 7j,k). This effect was especially strong for a fast calcium decay (< 100 ms) which is generally associated with nanodomains (Jarsky et al., 2010) rather than decay dynamics >>100 ms for microdomains (Beaumont et al., 2005). Clearly, a primary determinant for tuning a ribbon's high-frequency response is the local stimulus-driven calcium environment around the ribbon, rather than properties of the ribbon itself (see also (Baden et al., 2014, 2013a)). Nevertheless, once this is set, large pool sizes paired with a high release rate were generally preferable for all explored forms of signal detection. Taken together, our model therefore suggests that while the pre-synaptic calcium is a critical variable, even with a fixed calcium model the ribbon can be shifted into different response behaviours.

MATERIALS AND METHODS

Animals. All procedures were performed in accordance with the UK Animals (Scientific Procedures) act 1986 and approved by the animal welfare committee of the University of Sussex. Animals were housed under a standard 14:10 day/night rhythm and fed three times a day. Animals were grown in 0.1 mM 1-phenyl-2-thiourea (Sigma, P7629) from 1 *dpf* to prevent melanogenesis. For 2-photon *in-vivo* imaging, zebrafish larvae were immobilised in 2% low melting point agarose (Fisher Scientific, BP1360-100), placed on a glass coverslip and submerged in fish water. Eye movements were prevented by injection of a-bungarotoxin (1 nL of 2 mg/ml; Tocris, Cat: 2133) into the ocular muscles behind the eye.

For all experiments, we used *6-7 days post fertilization* (*dpf*) zebrafish (Danio rerio) larvae. The following previously published transgenic lines were used: *Tg(cx55.5:nlsTrpR)*, and *Tg(tUAS:SFiGluSnFR)* (Yoshimatsu et al., 2020b). In addition, *Tg(gnat2:SyjRGco1a)* lines were generated by injecting pTol2CG2-gnat2-SyjRGeco1a, plasmids into single-cell stage eggs. Injected fish were out-crossed with wild-type fish to screen for founders. Positive progenies were raised to establish transgenic lines.

The plasmid was made using the Gateway system (ThermoFisher, 12538120) with combinations of entry and destination plasmids as follows: pDESTtol2CG2 (Kwan et al., 2007), p5E-gnat2 (Lewis et al., 2010; Yoshimatsu et al., 2016), pME-SyjRGeco1a, p3E-pA. Plasmid pME-SyjRGeco1a was generated by inserting a polymerase chain reaction (PCR)-amplified jRGeco1a (Chen et al., 2013; Dana et al., 2016) into pME plasmid and subsequently inserting a PCR amplified zebrafish synaptophysin without stop codon at the 5' end of jRGeco1a.

EM. We used a previously published EM dataset of the larval zebrafish outer retina for this study (Yoshimatsu et al., 2020a). In the original paper, we only used one image stack from the acute zone, but here we

559　　　have in addition included two further stacks from nasal and dorsal
560　　　regions, respectively. Image stacks were concatenated and aligned
561　　　using TrackEM (NIH). The cones and ribbons were traced or painted
562　　　using the tracing and painting tools in TrackEM2 (Cardona et al., 2012).
563　　　Vesicle density on the ribbons was measured in 6 representative
564　　　sections per cone. We selected sections where ribbons were aligned
565　　　perpendicular to the sections. Ribbon release site length and area were
566　　　measured in the 3D reconstruction of the ribbons.

567　　　**2p imaging.** All 2-photon imaging was performed on a MOM-type 2-
568　　　photon microscope (designed by W. Denk, MPI, Martinsried; purchased
569　　　through Sutter Instruments/Science Products) equipped with a mode-
570　　　locked Ti:Sapphire laser (Chameleon Vision-S, Coherent) tuned to 980
571　　　nm. We used two fluorescence detection channels for iGluRSnFR
572　　　(F48x573, AHF/Chroma) and jRGeco1a (F39x628, AHF/Chroma), and a
573　　　water immersion objective (W Plan-Apochromat 20x/1,0 DIC M27,
574　　　Zeiss). For image acquisition, we used custom-written software (ScanM,
575　　　by M. Mueller, MPI, Martinsried and T. Euler, CIN, Tuebingen) running
576　　　under IGOR pro 6.3 for Windows (Wavemetrics). Recording
577　　　configuration was 124 x 32 pixels (2ms per line, 15.6 Hz). Light stimuli
578　　　were delivered through the objective, by band-pass filtered light emitting
579　　　diodes (LEDs, 'red' 588 nm, B5B-434-TY, 13.5cd, 8°, 20 mA; 'green'
580　　　477 nm, RLS-5B475-S; 3-4 cd, 15°, 20mA; 'blue' 415 nm, VL415-5-15;
581　　　10-16 mW, 15°, 20 mA; 'ultraviolet, UV' 365 nm, LED365-06Z; 5.5 mW,
582　　　4°, 20 mA, Roithner, Germany).

583　　　All LEDs were jointly further filtered using FF01-370/36 (AHF/Chroma)
584　　　and synchronized with the scan retrace at 500 Hz using a
585　　　microcontroller as described in (Zimmermann et al., 2020). The LED
586　　　intensity was 1.10^5, and 2.10^5 photons per cone per second for
587　　　adaptation period and UV flash, respectively, which corresponds to a
588　　　low-photopic regime. A stimulus time marker embedded in the recording
589　　　data was aligned the traces with a temporal precision of 2 ms. For all
590　　　experiments, animals were kept at constant background illumination for
591　　　at least 5 s at the beginning of each recording to allow for adaptation to
592　　　the laser. Regions of interest (ROIs), corresponding to individual
593　　　presynaptic terminals of UV-cones were defined manually. For calcium,
594　　　we restricted ROIs within 1 μm from the release site at a terminal, while
595　　　for glutamate we placed ROIs on the horizontal-cell dendrites
596　　　immediately adjacent to a given cone, as previously (Yoshimatsu et al.,
597　　　2020b). To unequivocally identify UV-cones, responses to the 'red',
598　　　'green', 'blue' and 'UV'-flashes were always recorded (always 1 s flash,
599　　　1 s darkness). Only cones that preferentially responded to the UV-LED
600　　　were kept for further analysis (Yoshimatsu et al., 2020a).

601　　　**Scaling and Denoising.** We preprocessed the recorded and z-scored
602　　　fluorescence traces as follows: First, we applied a linear baseline
603　　　correction to the calcium traces and then z-scored the calcium and
604　　　glutamate traces with respect to the mean and standard deviation of the

17

UV-bright stimulus intervals. By doing so we assumed that within these periods, calcium channels are closed, and recorded activity is either due to noise in the recording process or inherent channel/vesicle noise in the synapse. With this normalization, we achieved a similar scaling for all traces independent of the level of indicator expression. Based on these preprocessed data, the indices in Fig. 3c-j were computed.

For the model input, we further averaged each zone over the trials and then applied a Butterworth filter of order three with a cut-off frequency of 5 Hz to denoise the signals. Since the output of the model was in vesicles per second, we finally shifted the processed glutamate data by its minimal value such that it had only positive values. To use the calcium concentration as input to the model, we additionally applied a Wiener deconvolution with the kernel of the calcium indicator JRGeco1 to the data (assuming a SNR of 10 for $f < 1$Hz and a SNR of 1/20 for $f > 1$ Hz). The resulting pair of calcium/glutamate data per zone (Fig. 3a) was finally used in the subsequent model.

Data indices. *Maximal activation, Sustain and Transience:* To be less prone to noise we used the 90th- and 50th-percentiles (p_i) to calculate the maximal activation, transience and sustain:

$$\text{max} = p_{90}\left(x_{[t_0, t_1]}\right),$$

$$\text{sustain} = p_{50}\left(x_{[t_2, t_3]}\right),$$

$$\text{transience} = \frac{\text{max} - \text{sustain}}{\text{max}},$$

where x was the calcium/glutamate recording, respectively. The t_i were chosen such that the first (for *max*) or the last (for *sustained*) second after the onset of the dark period is included.

Off-, On-Detection index (I_{off}, I_{on}) and high frequency index (HFi): For the detection indices, we used a Gaussian noise stimulus $((\mu, \sigma) = (0.5, 0.3))$ with 2 Hz and a length of 150 s. This stimulus was shown for 120 s before the event to detect occurred with an amplitude of plus or minus four times the standard deviation and a duration of 500 ms. The detection indices of the simulation x were finally computed as

$$I_{off}(x) = \left(\text{max}\left(x_{[t_0, t_1]}\right) - \text{mean}\left(x_{[t_0, t_1]}\right)\right) / \text{std}\left(x_{[t_0, t_1]}\right),$$

$$I_{on}(x) = \text{abs}\left(\text{min}\left(x_{[t_0, t_1]}\right) - \text{mean}\left(x_{[t_0, t_1]}\right)\right) / \text{std}\left(x_{[t_0, t_1]}\right),$$

with $t_0 = 60$ s and $t_1 = 150$ s.

For the HF*i* we used uniformly distributed noise of 100 s at 20 Hz and computed the discretized power spectrum p of the simulation x with

Welch's method, and defined the HFi on the by the standard deviation normalized data x as

$$HFi(x) = \sum_{i=1}^{n} p_i(x) \cdot f_i \, ,$$

with n such that $f_n < 25$Hz.

Model. We modelled the synaptic release by a cascade-like ribbon synapse model (Fig. 4a) with three vesicle pools (reserve pool RP, intermediate pool IP and readily releasable pool RRP) and changing rates which were dependent on the occupancy of the pools (Baden et al., 2014; Sterling and Matthews, 2005). In this model, the glutamate release $e(t)$ was driven by the intracellular calcium $Ca(t)$:

$$e(t) = e_{max} \cdot f(Ca(t)) \cdot \frac{RRP(t)}{RRP_{max}}$$

with

$$f(Ca) = \frac{1}{1 + \exp(-k \cdot (Ca - x_0))} \, .$$

The changing rates $r(t)$ (between RP and IP) and $i(t)$ (between the IP and RRP) were independent of calcium:

$$r(t) = r_{max} \cdot \left(1 - \frac{IP(t)}{IP_{max}}\right) \cdot \frac{RP(t)}{RP_{max}}$$

$$i(t) = i_{max} \cdot \left(1 - \frac{RRP(t)}{RRP_{max}}\right) \cdot \frac{IP(t)}{IP_{max}}.$$

Additionally, the refilling $d(t)$ of the reserve pool was modelled by a constant factor of the available exocytosed vesicles $Exo(t)$:

$$d(t) = d_{max} \cdot Exo(t)$$

Therefore, the number of vesicles in the pools changed as:

$$\frac{dRP(t)}{dt} = d(t) - r(t)$$

$$\frac{dIP(t)}{dt} = r(t) - i(t)$$

$$\frac{dRRP(t)}{dt} = i(t) - e(t)$$

$$\frac{dExo(t)}{dt} = e(t) - d(t).$$

In the original model in (Baden et al., 2014) there was also a non-linear influence of calcium for $i(t)$ in terms of $\frac{Ca}{Ca+c}$. But initial runs of the fitting procedure resulted in $c \approx 0$ which indicated no calcium dependency for the changing rate i and we excluded this term in the presented model. Since the endocytosis constant d_{max} and the size of the reserve pool RP did not affect the output of the model, our fitting procedure was constrained to the remaining seven parameters: the changing rates (r_{max}, i_{max}, e_{max}) the non-linearity parameters (k and x_0), and the remaining pool sizes (IP and RRP). We call these parameters $\theta = (r_{max}, i_{max}, e_{max}, k, x_0, IP, RRP)$. From the equation above it follows that the model is scale invariant: a scaling of the parameters (except the parameters for the non-linearity, x_0 and k) results in a scaled model output and thus only an arbitrary scale in vesicle units (v.u.) to the experimental traces can be fitted.

The described coupled ODE was solved with *scipy*'s (version 1.5.1) implementation of the Bogacki–Shampine method (Bogacki and Shampine, 1989), an explicit Runge-Kutta method of order 3 with adaptive step-sizes, where the maximal step size was set to the step size of the (calcium) input signal.

Simplified Model. To reduce the parameter space to identify general rules or ribbon tuning (Fig. 6d-f, Fig. 7 and online tool) we fixed k to 10.2 (equal to the mean of the fitted parameters across zones) and additionally coupled the maximal changing rates to the pool sizes as follows:

$$r_{max} = 0.2 \cdot IP_{max}$$
$$i_{max} = 0.4 \cdot IP_{max}$$
$$e_{max} = \tilde{e}_{max} \cdot RRP_{max}$$

where $\tilde{e}_{max}$ can take values between 0 and 1.

For the general rules of ribbon tuning (Fig. 6d-f, Fig. 7 and online tool) the calcium concentration evoked by a light stimulus $s(t)$ is simulated as following:

$$Ca(t) = \kappa_2 * \exp(\kappa_1 * s(t))$$

where κ_1 is a biphasic kernel from (Baden et al., 2014) and κ_2 is a double exponential kernel with fixed time constant τ_{rise} (30 ms) and variable decay parameter τ_{decay}.

Parameter Inference. For the inference of the model parameters, we iterated the following steps over several rounds: First we draw samples from a prior, evaluated the model and extracted summary statistics on which the loss was computed. Based on these loss values and the sampled parameters a mixture of density network (MDN) was trained

20

and finally evaluated to get the posterior of this round which was used as the prior for the next round (Fig. 4b).

Summary statistics and discrepancy. A key ingredient in simulation-based Bayesian inference is to define problem and domain specific summary statistics to project the data to a low dimensional feature space. For our setting, we identified the following fourteen features x_i: baseline during adaption as well as period of UV-bright stimulus, mean during UV-dark period as well as mean of the maximal release rates in this periods, maximal and minimal (as maximal value and 25th percentile) amplitude during the first flash, maximal and minimal (as maximal value and 25th percentile) amplitude of the second peak, total number of released vesicles during first, second and the last activation.

To pay special attention to the decay after the initial UV-dark flash, which we found to be informative about the different pool sizes of the ribbon, we fitted an exponential decay to this period. We used the inferred time constant τ and the evaluation of the exponential function at the time point before the next light onset as additional features along with an extra penalty if an exponential rise instead of a decay was fitted.

To calculate the discrepancy D of a simulated trace e we normalized the features in each component with the mean and standard deviation of the recorded traces. We then took a weighted mean squared error of this normalized summary vector x to the normalized summary vector x_0 of the recorded trace as the discrepancy (*relevant loss*):

$$\mathcal{D}(e) = \frac{1}{14}\sum_{i=1}^{14} w_i \left(x_{0,i} - x_i\right)^2.$$

The weights w_i were not systematically optimized, but within reasonable ranges the results were relatively insensitive to the exact values. We chose w = (0.5,0.5,5,1,1,1,1,1,1,1,2,1,1,(0.01 for decay and 10·(1+ceil(τ)) for rise)) for the features in the order mentioned as above, where the last value is the extra penalty for the exponential rise instead of a decay.

Prior distribution and parameter normalization. The modes of the prior were chosen as *(r, i, e, k, x_0, IP_{max}, RRP_{max})* = (2.5, 2.5, 10, 14, 0.5, ≈13.8, ≈4.0), but as the model was scale invariant, the absolute values are uninformative and only the relative values are of interest. For technical reasons we normalized the prior distributions such that the means of the uncorrelated multivariate normal distribution were 0.5 and the standard deviations were 0.2 in each dimension. For the IP and RRP pool sizes, we additionally exponentially scaled the sampled parameters, such that no negative values could occur.

Parameter Inference. We applied the Sequential Neural Posterior Estimation method described in (Lueckmann et al., 2017) (code available at https://github.com/mackelab/delfi) (also called SNPE-B) with

some modifications which were also applied in (Oesterle et al., 2020; Yoshimatsu et al., 2020a). In brief, SNPE-B draws over several rounds samples $\{\theta_i\}_{i \in I}$ from a prior $\tilde{p}(\theta)$ and evaluates the model for these parameters. For each evaluation e_i the discrepancy function $x_i = \mathcal{D}(e_i)$ is computed and a mixture density network (MDN) $q_\phi(\theta, x)$ is trained on the data pairs $\{(\theta_i, x_i)\}_{i \in I}$. The posterior $p(\theta | x_0)$ is then calculated as $q_\phi(\theta | x = x_0)$ and used as a new prior $\tilde{p}(\theta)$ in the next sampling round. Instead of $x_0 = 0$ we calculated the new prior $\tilde{p}(\theta)$ in round n as $q_\phi(\theta | x = \beta_n)$ where β_n is the 0.1th percentile ρ of the discrepancy function of all samples. It turned out that this is an efficient way to get a more stable behavior of the MDN since it has not to extrapolate to unreached discrepancy values but is converging nevertheless. This evaluation of $q_\phi(\theta | x = \beta_n)$ at $\beta_n = \rho$ can be seen as the posterior over the parameters for the "best-possible" model evaluations. Testing for different percentiles in a reasonable range did not change the results. We took the same approach for setting an adaptive bandwidth for the kernel. As an additional post-hoc verification of the posteriors, we took as final posterior distributions the posterior of the round with the smallest median discrepancy of its samples ("early stopping").

Technical details. We ran the inference algorithm over 5 rounds, with 300.000 samples per round. We chose three Gaussian components for the mixture of Gaussian distribution and a MDN with two hidden layers with 120 nodes each. In each round the network was trained for 800 epochs with a minibatch size of 1000. To let the MDN focus on regions of low discrepancy, we used a combined half-uniform-half-Gaussian kernel which was constant up to the pseudo-observation β_n and decayed then as a half Gaussian. The scale of this half-Gaussian part of the kernel was in each round chosen as the 25th-percentile of the discrepancy function.

Sensitivity Analysis. Sensitivity analysis was performed using *uncertainpy* (Tennøe et al., 2018) by using the *GaussianMixture* probability distribution class of *chaospy* (Feinberg and Langtangen, 2015). Since model evaluations are computationally cheap and could run in parallel, we took the (quasi-) Monte Carlo Method with 10e5 samples, resulting in 450.000 simulations. With uncertainpy we calculated the first order Sobol sensitivity index S_i which is defined as

$$S_i = \frac{\mathbb{V}[\mathbb{E}[Y | \theta_i]]}{\mathbb{V}[Y]},$$

where $\mathbb{E}$ and $\mathbb{V}$ are the expected value and the variance, respectively. S_i measures the direct effect each parameter has on the variance of the model output (Saltelli et al., 2008; Tennøe et al., 2018). It tells us the expected reduction in relative variance if we fix parameter θ_i. The sum of the first-order Sobol indices cannot exceed one and is equal to one if

22

no interactions are present (Glen and Isaacs, 2012; Tennøe et al., 2018). We also calculated the total-order indices which gives the sensitivity due to interactions of the parameters. But since already the sum of the first-order indices is almost one for our model, the total order indices look quite similar and we omit their analysis.

It is important to remark, that the Sobol indices are not a way to show how 'important' parameters are. A parameter which is overbearingly influencing the model would in the limit of the posterior estimation accumulate the mass on one single point. But this means that for samples from the posterior this parameter is not responsible for any variance of the model output and thus its Sobol index would be zero. The Sobol indices are therefore the result of a complex interplay of the model and the posterior estimation, bur especially its temporal changes give us insight into the time dependent influence on the model output.

Linear baseline model. To evaluate the performance of the biophysical model, we compared it to a simple linear model. For this, we performed a regularized least square regression (ridge regression using *scikit-learn, version 0.23.1, https://scikit-learn.org)* to fit the calcium to glutamate response. In lack of a diverse enough dataset, we set the regularization coefficient alpha to 0.1 and allowed the model to include the data from the past 0.5 second to predict the next time point.

Statistical Analysis. We used Generalized Additive Models (GAMs) for the comparison of the vesicle densities (Fig. 1g, Fig. S1). GAMs are an extension to generalized linear models by allowing linear predictors that depend on smooth functions of the underlying variables (Wood, 2017). We used the mgcv-package (version 1.8-33) in R on an Windows 10 workstation with default parameters, if not specified differently below. We modelled the dependence of the vesicle density as a smooth term dependent on the distance with 100 degrees of freedom and grouped by "zone". We further used "zone" as additional predictive variable. The model explained ~65% of the deviance. Statistical significance for differences between the dependence on the vesicle density in the different retinal regions were obtained using the *plot_diff* function of the *itsadug*-package for R (version 2.4) with a 95% confidence level.

REFERENCES

Baden T, Euler T, Berens P. 2020. Understanding the retinal basis of vision across species. *Nat Rev Neurosci* **21**:5–20. doi:10.1038/s41583-019-0242-1

Baden T, Euler T, Weckström M, Lagnado L. 2013a. Spikes and ribbon synapses in early vision. *Trends Neurosci* **36**:480–8. doi:10.1016/j.tins.2013.04.006

Baden T, James B, Zimmermann MJYY, Bartel P, Grijseels D, Euler T, Lagnado L, Maravall M. 2018. Spikeling: A low-cost hardware implementation of a spiking neuron for neuroscience teaching and outreach. *PLoS Biol*. doi:10.1371/journal.pbio.2006760

Baden T, Nikolaev A, Esposti F, Dreosti E, Odermatt B, Lagnado L. 2014. A Synaptic Mechanism for Temporal Filtering of Visual Signals. *PLoS Biol* **12**:e1001972. doi:10.1371/journal.pbio.1001972

Baden T, Schubert T, Chang L Le, Wei T, Zaichuk M, Wissinger B, Euler T, Zaichuck M, Wissinger B,

23

845   Euler T, Zaichuk M, Wissinger B, Euler T. 2013b. A tale of two retinal domains: near-optimal
846   sampling of achromatic contrasts in natural scenes through asymmetric photoreceptor
847   distribution. *Neuron* **80**:1206–17. doi:10.1016/j.neuron.2013.09.030

848   Beaumont V, Llobet A, Lagnado L. 2005. Expansion of calcium microdomains regulates fast
849   exocytosis at a ribbon synapse. *Proc Natl Acad Sci U S A* **102**:10700–5.
850   doi:10.1073/pnas.0501961102

851   Bellono NW, Leitch DB, Julius D. 2018. Molecular tuning of electroreception in sharks and skates.
852   *Nature* **558**:122–126. doi:10.1038/s41586-018-0160-9

853   Bogacki P, Shampine LF. 1989. A 3(2) pair of Runge - Kutta formulas. *Appl Math Lett.*
854   doi:10.1016/0893-9659(89)90079-7

855   Cardona A, Saalfeld S, Schindelin J, Arganda-Carreras I, Preibisch S, Longair M, Tomancak P,
856   Hartenstein V, Douglas RJ. 2012. TrakEM2 Software for Neural Circuit Reconstruction. *PLoS*
857   *One* **7**:e38011. doi:10.1371/journal.pone.0038011

858   Chen T-W, Wardill TJ, Sun Y, Pulver SR, Renninger SL, Baohan A, Schreiter ER, Kerr RA, Orger MB,
859   Jayaraman V, Looger LL, Svoboda K, Kim DS. 2013. Ultrasensitive fluorescent proteins for
860   imaging neuronal activity. *Nature* **499**:295–300. doi:10.1038/nature12354

861   Dana H, Mohar B, Sun Y, Narayan S, Gordus A, Hasseman JP, Tsegaye G, Holt GT, Hu A, Walpita
862   D, Patel R, Macklin JJ, Bargmann CI, Ahrens MB, Schreiter ER, Jayaraman V, Looger LL,
863   Svoboda K, Kim DS. 2016. Sensitive red protein calcium indicators for imaging neural activity.
864   *Elife* **5**. doi:10.7554/eLife.12727

865   DeVries SH, Li W, Saszik S. 2006. Parallel processing in two transmitter microenvironments at the
866   cone photoreceptor synapse. *Neuron* **50**:735–48. doi:10.1016/j.neuron.2006.04.034

867   Feinberg J, Langtangen HP. 2015. Chaospy: An open source tool for designing methods of
868   uncertainty quantification. *J Comput Sci.* doi:10.1016/j.jocs.2015.08.008

869   Franceschini N, Hardie R, Ribi W, Kirschfeld K. 1981. Sexual dimorphism in a photoreceptor. *Nature.*
870   doi:10.1038/291241a0

871   Glen G, Isaacs K. 2012. Estimating Sobol sensitivity indices using correlations. *Environ Model Softw.*
872   doi:10.1016/j.envsoft.2012.03.014

873   Gonçalves PJ, Lueckmann JM, Deistler M, Nonnenmacher M, Öcal K, Bassetto G, Chintaluri C,
874   Podlaski WF, Haddad SA, Vogels TP, Greenberg DS, Macke JH. 2020. Training deep neural
875   density estimators to identify mechanistic models of neural dynamics. *Elife.*
876   doi:10.7554/ELIFE.56261

877   Gutenkunst RN, Waterfall JJ, Casey FP, Brown KS, Myers CR, Sethna JP. 2007. Universally sloppy
878   parameter sensitivities in systems biology models. *PLoS Comput Biol.*
879   doi:10.1371/journal.pcbi.0030189

880   Hays C, Sladek A, Field G, Thoreson W. 2021. Properties of multi-vesicular release from rod
881   photoreceptors support transmission of single photon responses. *bioRxiv* 2021.02.01.429179.
882   doi:10.1101/2021.02.01.429179

883   Holler S, Köstinger G, Martin KAC, Schuhknecht GFP, Stratford KJ. 2021. Structure and function of a
884   neocortical synapse. *Nature* 1–6. doi:10.1038/s41586-020-03134-2

885   Jackman SL, Choi S-Y, Thoreson WB, Rabl K, Bartoletti TM, Kramer RH. 2009. Role of the synaptic
886   ribbon in transmitting the cone light response. *Nat Neurosci* **12**:303–10. doi:10.1038/nn.2267

887   Jarsky T, Tian M, Singer JH. 2010. Nanodomain control of exocytosis is responsible for the signaling
888   capability of a retinal ribbon synapse. *J Neurosci* **30**:11885–95. doi:10.1523/JNEUROSCI.1415-
889   10.2010

890   Kwan KM, Fujimoto E, Grabher C, Mangum BD, Hardy ME, Campbell DS, Parant JM, Yost HJ, Kanki
891   JP, Chien C-B. 2007. The Tol2kit: A multisite gateway-based construction kit forTol2 transposon
892   transgenesis constructs. *Dev Dyn* **236**:3088–3099. doi:10.1002/dvdy.21343

24

893   Land MF, Nilsson D-E, Nilson D-E, Nilsson D-E. 2012. Animal Eyes. Oxford University Press.
894   doi:10.1093/acprof:oso/9780199581139.001.0001

895   Lewis A, Williams P, Lawrence O, Wong ROL, Brockerhoff SE. 2010. Wild-type cone photoreceptors
896   persist despite neighboring mutant cone degeneration. *J Neurosci.*
897   doi:10.1523/JNEUROSCI.5019-09.2010

898   Lueckmann JM, Gonçalves PJ, Bassetto G, Öcal K, Nonnenmacher M, Mackey JH. 2017. Flexible
899   statistical inference for mechanistic models of neural dynamicsAdvances in Neural Information
900   Processing Systems.

901   Moser T, Grabner CP, Schmitz F. 2019. Sensory processing at ribbon synapses in the retina and the
902   cochlea. *Physiol Rev* physrev.00026.2018. doi:10.1152/physrev.00026.2018

903   Oesterle J, Behrens C, Schröder C, Herrmann T, Euler T, Franke K, Smith RG, Zeck G, Berens P.
904   2020. Bayesian inference for biophysical neuron models enables stimulus optimization for retinal
905   neuroprosthetics. *Elife* **9**:1–38. doi:10.7554/eLife.54997

906   Regus-Leidig H, Brandstätter JH. 2012. Structure and function of a complex sensory synapse. *Acta*
907   *Physiol.* doi:10.1111/j.1748-1716.2011.02355.x

908   Saltelli A, Ratto M, Andres T, Campolongo F, Cariboni J, Gatelli D, Saisana M, Tarantola S. 2008.
909   Global Sensitivity Analysis. The Primer, Global Sensitivity Analysis. The Primer.
910   doi:10.1002/9780470725184

911   Schnapf JL, Baylor DA. 1987. How photoreceptor cells respond to light. *Sci Am* **256**:40–7.

912   Schröder C, James B, Lagnado L, Berens P. 2019. Approximate Bayesian inference for a mechanistic
913   model of vesicle release at a ribbon synapseAdvances in Neural Information Processing
914   Systems.

915   Sinha R, Hoon M, Baudin J, Okawa H, Wong ROL, Rieke F. 2017. Cellular and Circuit Mechanisms
916   Shaping the Perceptual Properties of the Primate Fovea. *Cell* **168**:413-426.e12.
917   doi:10.1016/j.cell.2017.01.005

918   Sterling P, Matthews G. 2005. Structure and function of ribbon synapses. *Trends Neurosci* **28**:20–9.
919   doi:10.1016/j.tins.2004.11.009

920   Szatko KP, Korympidou MM, Ran Y, Berens P, Dalkara D, Schubert T, Euler T, Franke K. 2019.
921   Neural circuits in the mouse retina support color vision in the upper visual field. *bioRxiv* 745539.
922   doi:10.1101/745539

923   Tennøe S, Halnes G, Einevoll GT. 2018. Uncertainpy: A Python Toolbox for Uncertainty
924   Quantification and Sensitivity Analysis in Computational Neuroscience. *Front Neuroinform.*
925   doi:10.3389/fninf.2018.00049

926   Wichmann C, Moser T. 2015. Relating structure and function of inner hair cell ribbon synapses. *Cell*
927   *Tissue Res* **361**:95–114. doi:10.1007/s00441-014-2102-7

928   Wood SN. 2017. Generalized additive models: an introduction with R. CRC press.

929   Yoshimatsu T, Bartel P, Schröder C, Janiak FK, St-Pierre F, Berens P, Baden T. 2020a. Near-optimal
930   rotation of colour space by zebrafish cones in vivo. *bioRxiv.*

931   Yoshimatsu T, D'Orazi FD, Gamlin CR, Suzuki SC, Suli A, Kimelman D, Raible DW, Wong RO. 2016.
932   Presynaptic partner selection during retinal circuit reassembly varies with timing of neuronal
933   regeneration in vivo. *Nat Commun* **7**. doi:10.1038/ncomms10590

934   Yoshimatsu T, Schröder C, Nevala NE, Berens P, Baden T. 2020b. Fovea-like Photoreceptor
935   Specializations Underlie Single UV Cone Driven Prey-Capture Behavior in Zebrafish. *Neuron.*
936   doi:10.1016/j.neuron.2020.04.021

937   Zimmermann MJY, Maia Chagas A, Bartel P, Pop S, Prieto-Godino LL, Baden T. 2020. LED
938   Zappelin': An open source LED controller for arbitrary spectrum visual stimulation and
939   optogenetics during 2-photon imaging. *HardwareX.* doi:10.1016/j.ohx.2020.e00127

940

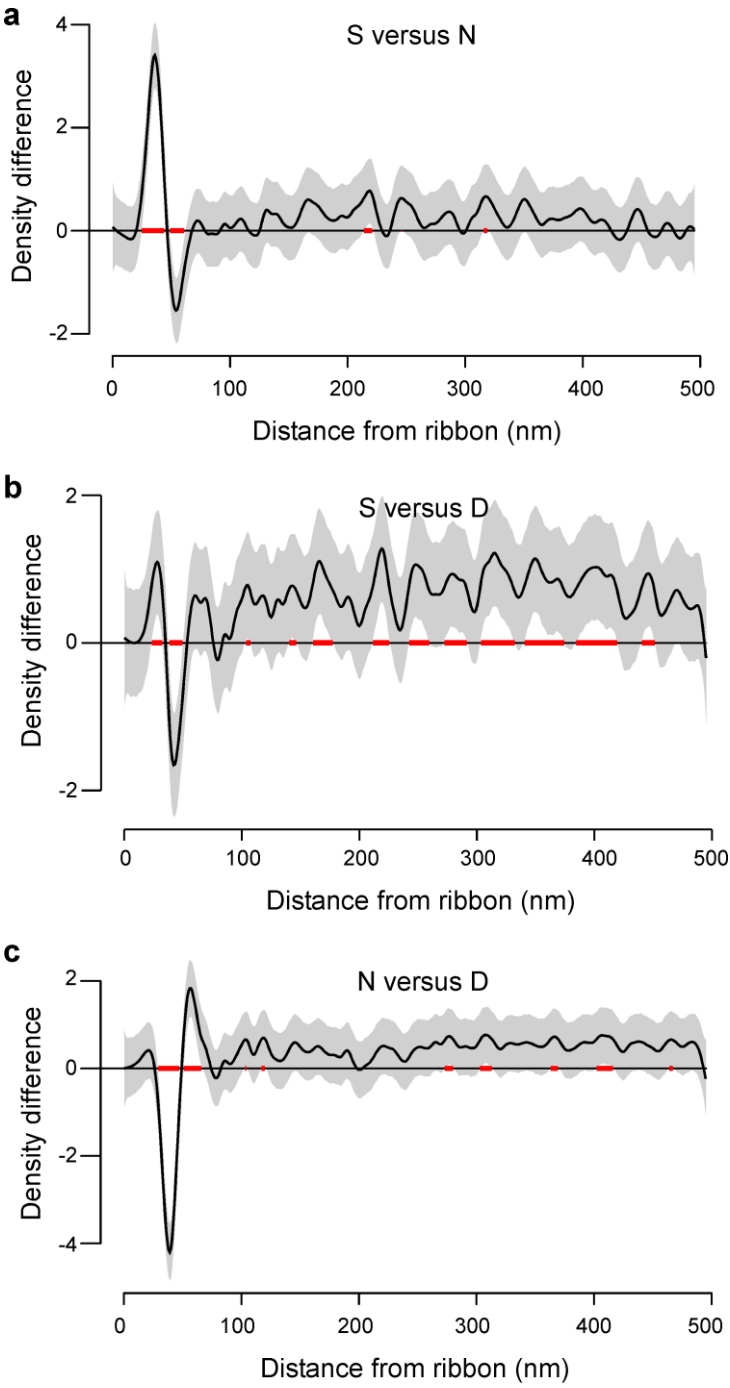941   **SUPPLEMENTARY FIGURES 1-3**

942

943   ***Figure S1 Statistical comparison of spatial vesicle distributions. a-c,*** *Pair-wise comparison of the three*
944   *regions, modelled as General Additive Model (Methods). The estimated mean difference (black) and 95%*
945   *confidence intervals (grey) are shown and significant differences (α=0.05) are highlighted (red).*
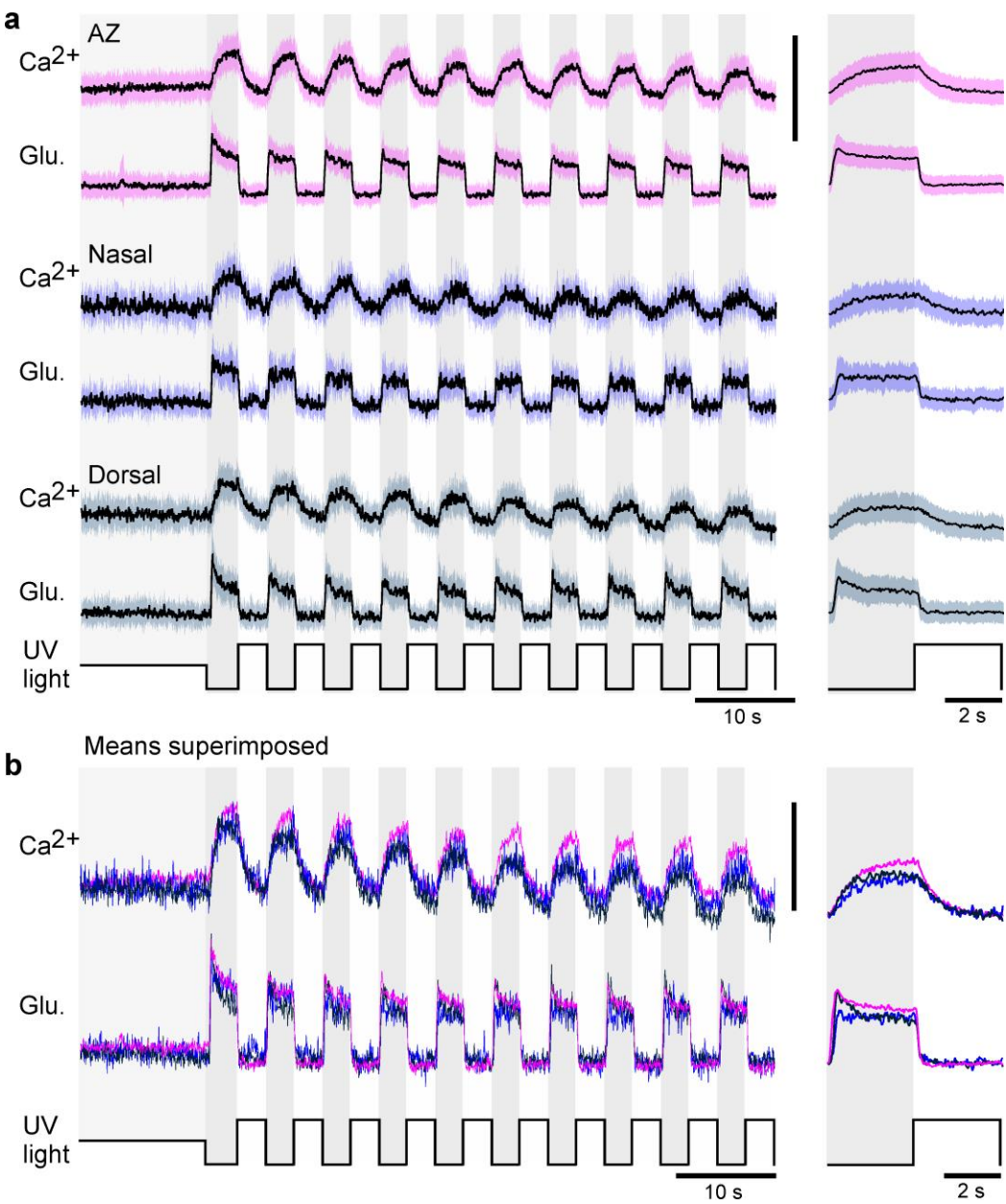
Figure S2. Mean calcium and glutamate traces per region. a, Z-scored recordings before scaling and de-noising (mean±SD). **b,** Superimposed means of the data shown in (a).
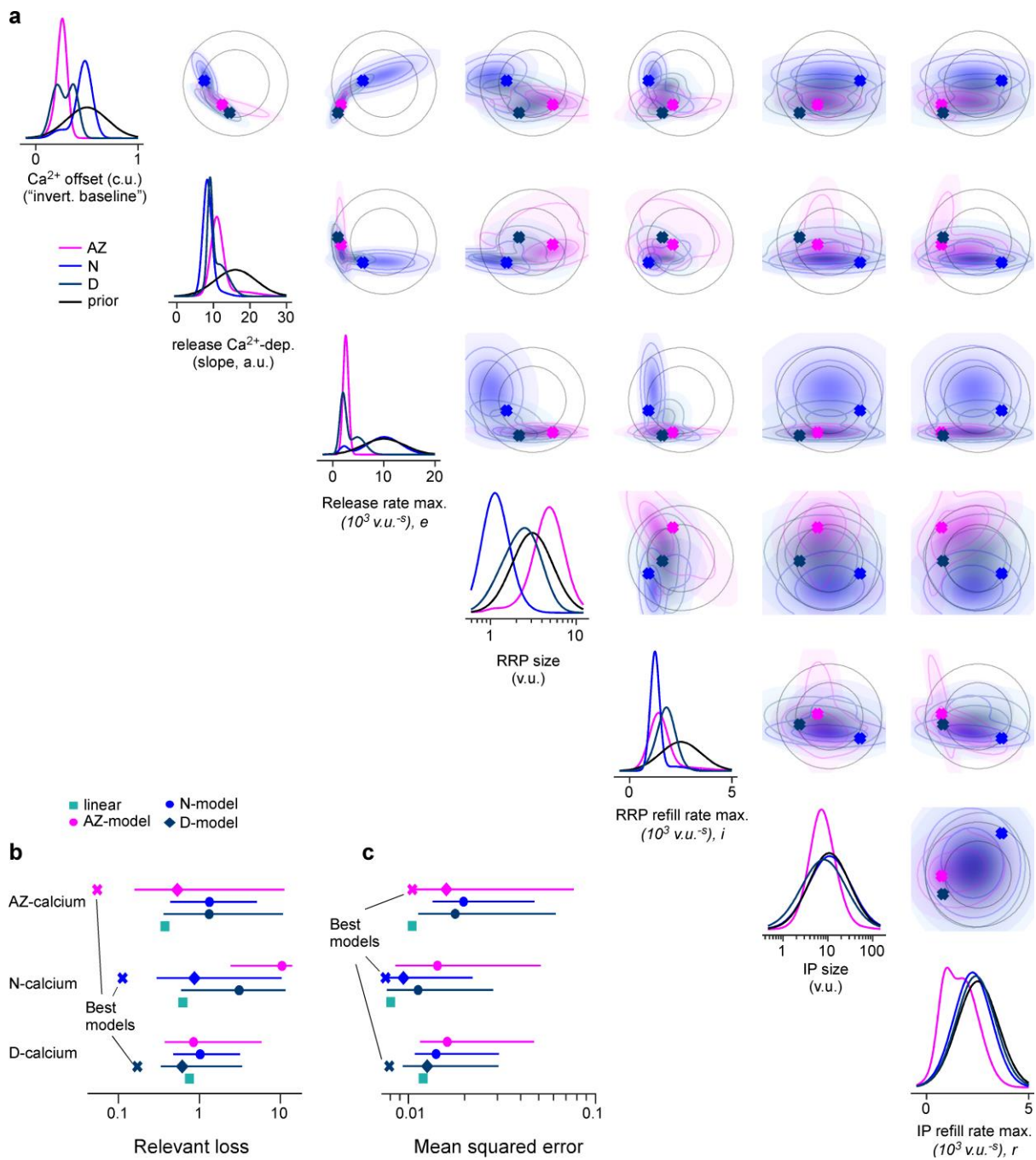
Figure S3. a, One- and two-dimensional marginals of the posterior as well as of the prior. Best parameters per region are marked as a cross. **b,** Median with 5th and 95th-percentiles (error bars) for the relevant loss based on the summary statistics (Methods), as well as the loss for the best zone specific and the linear baseline model for comparison. **c,** Same as (b) but loss as Mean Squared Error (MSE) between glutamate recordings and model output.